137 (2022) 212807

Contents lists available at ScienceDirect

Biomaterials Advances

journal homepage: www.journals.elsevier.com/materials-science-and-engineering-c

# 3D printing with star-shaped strands: A new approach to enhance *in vivo* bone regeneration

Yago Raymond [a,b,c,d], Cyril Lehmann [a,b], Emilie Thorel [d], Raúl Benitez [c,e], Antonio Riveiro [f], Juan Pou [g], Maria-Cristina Manzanares [h], Jordi Franch [i], Cristina Canal [a,b,c], Maria-Pau Ginebra [a,b,c,j,*,1]

[a] *Biomaterials, Biomechanics and Tissue Engineering Group, Department of Materials Science and Engineering, Universitat Politècnica de Catalunya (UPC), EEBE, Av. Eduard Maristany, 16, 08019 Barcelona, Spain*
[b] *Barcelona Research Centre for Multiscale Science and Engineering, Universitat Politècnica de Catalunya (UPC), EEBE, Av. Eduard Maristany, 10-14, 08019 Barcelona, Spain*
[c] *Biomedical Engineering Research Center (CREB), Universitat Politècnica de Catalunya, Av. Diagonal, 647, 08028 Barcelona, Spain*
[d] *Mimetis Biomaterials S.L., Carrer de Cartagena, 245, 3F, 08025 Barcelona, Spain*
[e] *Institut de Recerca Sant Joan de Déu (IRSJD), 39-57, 08950 Esplugues del Llobregat (Barcelona), Spain*
[f] *Department of Materials Engineering, Applied Mechanics and Construction, University of Vigo (UVigo), EEI, Lagoas-Marcosende, 36310 Vigo, Spain*
[g] *Department of Applied Physics, University of Vigo (UVigo), EEI, Lagoas-Marcosende, 36310 Vigo, Spain*
[h] *Human Anatomy and Embryology Unit, Department of Pathology and Experimental Therapeutics, Universitat de Barcelona, 08907 L'Hospitalet de Llobregat (Barcelona), Spain*
[i] *Bone Healing Group, Small Animal Surgery Department, Veterinary School, Universitat Autònoma de Barcelona, 08193 Bellaterra (Barcelona), Spain*
[j] *Institute for Bioengineering of Catalonia (IBEC), Barcelona Institute of Science and Technology, Baldiri Reixac 10-12, 08028 Barcelona, Spain*

ARTICLE INFO

*Keywords:*
3D printing
Bone regeneration
Scaffold
Pore architecture
Biomimetic calcium phosphate
*In vivo*

ABSTRACT

Concave surfaces have shown to promote bone regeneration *in vivo*. However, bone scaffolds obtained by direct ink writing, one of the most promising approaches for the fabrication of personalized bone grafts, consist mostly of convex surfaces, since they are obtained by microextrusion of cylindrical strands. By modifying the geometry of the nozzle, it is possible to print 3D structures composed of non-cylindrical strands and favor the presence of concave surfaces. In this work, we compare the *in vivo* performance of 3D-printed calcium phosphate scaffolds with either conventional cylindrical strands or star-shaped strands, in a rabbit femoral condyle model. Monocortical defects, drilled in contralateral positions, are randomly grafted with the two scaffold configurations, with identical composition. The samples are explanted eight weeks post-surgery and assessed by μ-CT and resin-embedded histological observations. The results reveal that the scaffolds containing star-shaped strands have better osteoconductive properties, guiding the newly formed bone faster towards the core of the scaffolds, and enhance bone regeneration, although the increase is not statistically significant ($p > 0.05$). This new approach represents a turning point towards the optimization of pore shape in 3D-printed bone grafts, further boosting the possibilities that direct ink writing technology offers for patient-specific applications.

## 1. Introduction

The increasing development of additive manufacturing technologies has allowed, in recent years, the introduction of personalized medicine strategies in the field of bone regeneration [1]. Calcium phosphates (CaP) are among the best performing materials for this application, due to their similarity to the mineral phase of bone [2]. Biomimetic hydroxyapatite (HA) processed under physiological conditions outstands, as it accurately mimics the bone composition and microstructure [3].

A wide variety of additive manufacturing techniques have been used

* Corresponding author at: Biomaterials, Biomechanics and Tissue Engineering Group, Department of Materials Science and Engineering, Universitat Politècnica de Catalunya (UPC), EEBE, Av. Eduard Maristany, 16, 08019 Barcelona, Spain.
*E-mail address:* maria.pau.ginebra@upc.edu (M.-P. Ginebra).
[1] Present address: Department of Materials Science and Engineering, Universitat Politècnica de Catalunya (UPC), EEBE, Av. Eduard Maristany, 16, 08019 Barcelona, Spain.

https://doi.org/10.1016/j.bioadv.2022.212807
Received 21 September 2021; Received in revised form 14 March 2022; Accepted 12 April 2022
Available online 18 April 2022

to print CaP 3D bone scaffolds [4]. Among them, filamentary-based direct ink writing (DIW) consists of extruding a pseudoplastic ink through a nozzle and controlling the deposition coordinates in order to generate, layer by layer, the desired 3D structure [5]. Different ink formulations have been proposed, and amongst them, those using a hydrogel as a carrier for the ceramic powder present several advantages [6]. In addition to allow a high volume fraction of ceramic particles, they are compatible with the use of reactive powders, which are at the origin of the self-hardening ceramic inks. In this case, the consolidation of the ceramic scaffold is not based on a high-temperature sintering process, but on a cement-like reaction that leads to the hardening of the structure at body temperature [7,8]. In contrast to high-temperature sintering, this mild consolidation setting can be combined with strategies involving biological molecules or even cells [9,10].

The role of macro and micro porosity in the bone regeneration is a controversial topic and it is difficult to establish universal criteria, in part because these parameters cannot be considered independently of other factors such as pore geometry, textural properties or material composition. While some studies conclude that macropore [11] and micropore size [12] have hardly any effect on the *in vivo* performance, others argue that there is an optimal macropore size range. While the optimal range has traditionally been fixed to 300–500 μm, a recent study suggests higher values, ranging from 700 to 1200 μm [13]. In any case, macropore size needs to be larger than ~50–100 μm to allow the penetration of blood vessels [14,15]. Beyond the influence of pore size, what is clear is that interconnected macroporosity is required for scaffold vascularization and colonization by the host tissue, and micropores are key for their interaction with bone at a cellular level [14,16,17].

Besides pore size and pore interconnectivity, pore morphology also plays an important role in the biological performance of bone scaffolds. Numerous studies have demonstrated that the concavity of a surface is a determining factor in its ability to trigger bone formation [17–27]. For example, when comparing 3D-printed CaP scaffolds to foamed architectures with the same composition, despite the excellent osteoconductivity of both sample types, superior osteoinductive properties were found for the foamed samples when tested ectopically [28], which resulted also in higher osteogenesis also orthotopically [29]. This highlights the role played by pore architecture, and more specifically, by the type of surface curvature that predominates in each kind of the pore geometry, convex surfaces in the case of the 3D-printed filaments, and concave surfaces for the foams. However, the underlying mechanisms are still unclear. Some studies relate this phenomenon with the microenvironments created within the concavities of the pores, which may favor the differentiation of mesenchymal stem cells to osteoblasts [20–23,30]. As they are protected from the flow of physiological fluids, the concentrations of soluble species, both proteins, and ions, in the concave regions may be different from those in their environment. For instance, in the case of calcium phosphate substrates, supersaturation levels of calcium and phosphate ions may be reached, due to the dissolution or cell-mediated resorption of the scaffold. This, combined with the material capabilities of adsorbing endogenous molecular signals, may trigger the differentiation of the cells towards osteogenic lineages. Other investigations, rather than focusing on chemical factors, attribute the curvature-driven tissue growth to physical or mechanical factors [19,24–27]. Namely, tissue growth is influenced by the curvature of the subjacent surface, since the way how cells apply forces and the tension developing in cell networks depends on the geometry of the substrate. Globally, the underlying physics would be analogous to that which governs processes as different as crystal growth, phase transformation, membrane mechanics, or surface-wetting by viscous liquids where the tendency to minimize the system's energy results in the nucleation/accumulation occurring in the regions with the lowest curvature radium and therefore lowest surface energy.

As previously mentioned, DIW has many advantages, including the possibility of tailoring both the external geometry and the internal porosity of the scaffolds [31–34]. However, the convex nature of the printed filaments, as circular nozzles are typically used, is a drawback when considering osteoinduction and bone formation. To overcome this limitation, in a recent work we developed for the first time 3D-printed CaP scaffolds with non-convex strand surfaces [35]. Briefly, custom-made non-circular nozzles were used to print strands with different cross-section geometries instead of the traditional cylindrical shape. A self-setting hydrogel-based alpha tricalcium phosphate (α-TCP) ink was used, which allowed to fabricate calcium deficient hydroxyapatite (CDHA) scaffolds with different filament morphologies. Nevertheless, the impact of filament geometry on their *in vivo* performance is still unknown. The present study aims to compare the *in vivo* performance of structures composed of strands with added concave surfaces obtained using a four-pointed-star nozzle (coded as S-scaffolds, which stands for star-shaped) to architectures based on traditional cylindrical strands (C-scaffolds), in a rabbit femoral condyle model.

## 2. Materials and methods

### 2.1. Scaffolds fabrication

A powder phase of α-TCP was mixed with a hydrogel consisting of a poloxamer 407 aqueous solution as described elsewhere [33]. The resulting ink was extruded through a custom-made direct ink writing device. Scaffolds with cylindrical strands (C-scaffolds) were printed with a commercial nozzle with a circular orifice of 410 μm (22ga Tappered Tip, Fisnar, WI, USA). To produce scaffolds with star-shaped strands (S-scaffolds) a custom-made modular nozzle was used, as described in previous work [35], which had a four-point star-shaped orifice, and resulted in star-shaped strands. The cross-section area was very similar for the two strand geometries (0.12 and 0.13 $mm^2$ for the C and S strands, respectively) [35]. The scaffolds were printed with an orthogonal fill pattern consisting of 90° alternated deposition orientation in the XY printing plane and a theoretical infill percentage of 62%. That corresponded to an interstrand separation in the printing plane of 251 and 227 μm for the C and S scaffolds, respectively. Scaffolds with two different geometries were printed: (1) Cylindrical samples with 8 mm in diameter and height, which were used after grinding to 5-mm diameter for the *in vivo* study and material characterization. (2) For mechanical testing, 8 mm-side cubic samples were fabricated and tested either directly or after grinding to 7 mm-side cubes.

The as-printed scaffolds were subjected to a hydrothermal hardening process, comprising a first step of vapor pre-treatment followed by an autoclaving step immersed in water, as described in previous work [33]. Afterward, the samples were water-sanded with P1200-grain sandpaper to obtain 5 mm-diameter cylinders and 7 mm-side cubic samples. Grinding was performed to remove the irregularities of the lateral faces of the scaffolds, where the filaments change direction. In this way, only the regular structure of the scaffold was retained, in order to better capture the effect of the strand geometry. After grinding, the specimens were sonicated in distilled water in three successive 5-minute washing steps to eliminate possible remaining sanded particles. Then, they were packaged in double sterilization pouches and sterilized by wet heat in an autoclave.

### 2.2. Material characterization

#### 2.2.1. Composition and microstructure

The composition of the scaffolds was characterized by X-ray diffraction (XRD) and Fourier-transform infrared (FTIR) spectroscopy. Prior to analysis, the samples were grinded in an agate mortar. The X-ray diffractograms were acquired with a diffractometer (D8 Advance, Bruker, Kontich, Belgium) equipped with a Cu Kα X-ray tube operated at 40 kV and 40 mA. Data were collected at 0.02° $step^{-1}$ over the 2θ range 10–80°. Additionally, the amorphous content and the crystalline phases were quantified by Rietveld refinement adding an external standard (corundum, ICSD-033639) to the powder, that was analyzed in a

diffractometer (D8 Advance Eco, Bruker AXS GmbH, Karlsruhe, Germany) equipped with a Cu K-α beam, a Ni filter and a LynxEye detector scanning the 3–65° 2θ range with a step size of 0.02°. Two phases, additional to the external standard, were identified and quantified: calcium deficient hydroxyapatite (COD-9002214) and β-tricalcium phosphate (ICSD-006191). KBr-FTIR spectroscopy was performed by analyzing hydraulic pressed pellets prepared from a mixture of 2 mg of sample and 300 mg of KBr. The spectrometer (Nicolet 6700, Thermo Fisher, MA, USA) scanned the sample absorbance along the wavelength spectra of 4000 to 400 $cm^{-1}$ with a step resolution of 2 $cm^{-1}$ and an accumulation of 256 scans per sampling step.

The microstructure of the samples was observed with a scanning electron microscope (FIB/SEM, Neon 40, Zeiss, Oberkochen, Germany) operated at 5 kV using a through-the-lens electron detector. Previously, the samples were coated by sputter deposition with a thin electron-conductive carbon layer before its analysis.

#### 2.2.2. Porosity and specific surface area

All the scaffolds prepared for the *in vivo* study were imaged by X-ray micro-computed tomography (μ-CT) prior to implantation. The images were acquired with the same machine setup used later for the explanted samples (explained in detail in the next section). However, as the high contrast between regions allowed it, the resolution was lowered to 18 μm $pixel^{-1}$, the scan rotation was set to 180° and a frame averaging of 1 was used to reduce the acquisition time. The resulting data were reconstructed in the same way as for the explanted samples, and 3D renders were performed (CTvox v3.2.0 software, Bruker, Kontich, Belgium). The scaffolds were aligned to the cartesian axes and a volume of interest (VOI) of 5 repetition units in the three orthogonal axes was selected (DataViewer v1.5.2.4 software, Bruker, Kontich, Belgium). The reconstructions were segmented and the macroporosity percentage ($P_{macro}$) was determined (CTAn v1.12.0 software, Bruker, Kontich, Belgium). Additionally, this software allowed to quantify the scaffold envelope surface and to calculate the specific surface area normalized by material volume (MV) (*i.e.*, MS/MV) and by strand length (*i.e.*, MS/strand mm).

Helium pycnometry (AccuPyc 1330, Micromeritics, GA, USA) was used to determine the skeletal density ($\rho_{skel}$) of the bulk material, and the apparent density ($\rho_{app}$) of the specimens was determined by measuring with a caliper the volume of cubic samples and weighting them (after drying overnight at 60 °C in a stove). Both densities were combined as previously described by Pastorino *et al.* to determine the sample's total porosity ($P_{tot}$) by gravimetric routes [36]. The open porosity and pore entrance size distribution in the 0.006–360 μm range were measured by mercury intrusion porosimetry (MIP, AutoPore IV Micromeritics, GA, USA). Finally, the percentage of microporosity inside the strands was estimated from the MIP results and skeletal density measurements (Eq. (1)). First, the specific volume of micropores ($V_{micro\ (<10\mu m)}$, established as pores below 10 μm) was measured as the volume of mercury intruded in the pores with sizes comprised between 0.006 and 10 μm per gram of material. Then the specific material volume ($V_{mat}$) was calculated as the inverse of the skeletal density. Finally, the porosity inside the strands was obtained from the following equation:

$$P_{micro} = \left(\frac{V_{micro\ (\langle 10\mu m)}}{V_{micro\ (\langle 10\mu m)} + V_{mat}}\right) \bullet 100 = \left(\frac{V_{micro\ (\langle 10\mu m)}}{V_{micro\ (\langle 10\mu m)} + {}^{1}/_{\delta_{sk}}}\right) \bullet 100 \quad (1)$$

The specific surface area ($SSA_{BET}$) of both scaffold types was determined by nitrogen adsorption (ASAP 2020, Micromeritics, GA, USA) using the Brunauer-Emmett-Teller (BET) method. Samples were previously outgassed in a vacuum atmosphere (10 mmHg) for 2 h at 100 °C.

#### 2.2.3. Mechanical properties

The ultimate compressive strength (UCS) and the Weibull modulus of the scaffolds were assessed by uniaxial compressive testing (Bionix 858 uniaxial, MTS systems, MN, USA) under displacement-control conditions at a rate of 1 mm $min^{-1}$ and using a load cell of 2.5 KN. C- and S-cubic scaffolds were tested, with polished or unpolished lateral faces (*i.e.* 8-mm side or 7-mm side cubes, respectively), with fifteen replicates per group. The specimens were immersed in water 1 h before the experiment and tested in wet conditions to better replicate the behavior in a physiological environment.

The Weibull modulus was calculated by applying the Weibull probability distribution equation (Eq. (2)) to the obtained UCS of the samples, where $P_s$ corresponds to the survival probability of the sample, $\sigma$ corresponds to the UCS, $\sigma_0$ is a constant that represents the stress at which all the samples will survive and $m$ corresponds to the Weibull modulus.

$$ln\left(ln\left(\frac{1}{P_s}\right)\right) = m(ln(\sigma) - ln(\sigma_0)) \quad (2)$$

### 2.3. Animals

Adult New Zealand White (NZW) rabbits with an age ranging from 8 to 12 months and a bodyweight ranging from 4.8 to 5.5 Kg were used. The animals were purchased from a professional stock breeder (Charles River, Saint Aubin les Elboeuf, France) and housed in individual 2 $m^2$ boxes during the course of the study. Prior to the surgery, a two-week acclimatization period was established.

### 2.4. Study design

The procedure was conducted in compliance with the European Community Guidelines (Directive 2010/63/EU) and the Guide for Care and Use of Laboratory Animals [37]. The study, which was part of a larger project to analyze the bone regeneration capacity of scaffolds with different configurations, obtained the permission of the local Animal Ethics Committee for Human and Animal Experimentation (Approval number: CEAAH 4683). A total of seven animals were used. A circular monocortical osteochondral defect was drilled bilaterally (2 defects per animal) in the medial aspect of the femoral condyle. The bone regeneration potential of the scaffolds with star-shaped strands was compared to a positive control group of scaffolds with cylindrical strands. For each animal one scaffold of each condition (S or C) was randomly grafted in the left or right femur condyle. The outcome was evaluated 8 weeks post-surgery and consisted of a μ-CT volumetric assessment and a qualitative histological assessment of the scaffolds' cross-sections.

### 2.5. Surgical procedure

The surgical procedure was performed under standard sterile conditions. After sedation, the animals were anesthetized with propofol and maintained with inhaled isoflurane (2%) in an oxygen carrier by mask. After aseptic preparation of the surgical site, the animals were placed in a dorsal recumbent position and a bilateral medial parapatellar skin incision was performed to expose the medial aspect of both femoral condyles. A first mono-cortical cylindrical defect with a depth of 10 mm was created in the center of the femur condyle by using Ø2.5 mm drill bit under copious saline solution irrigation to avoid thermal necrosis. Next, the defect was expanded to Ø5 mm. The defects were grafted with press-fitted cylindrical scaffolds of 5 mm in diameter and 10 mm in height. Two different scaffold conditions were used (C and S). Afterward, the surgical wound was sutured in consecutive layers. Anesthetic recovery of the animals was uneventful. At eight weeks post-surgery, the animals were euthanized with a sodium pentobarbital overdose in compliance with the American Veterinary Medical Association legislation. Immediately after euthanasia, the condylar regions were explanted and fixed in neutral buffered formalin solution (10%) for two weeks and dehydrated in an increasing series of ethanol solutions.

### 2.6. Histomorphometric assessment

#### 2.6.1. Micro-computed tomography acquisition

The dehydrated samples were analyzed by μ-CT (Skyscan 1272, Bruker, Kontich, Belgium). The tomographic measurements were performed with an acceleration voltage of 90 kV and an X-ray current of 111 μA. The X-ray spectrum of the tungsten target was modified by using a 0.5 mm-thick aluminum filter and a 0.038 mm-thick copper filter. The exposure time per projection was 2600 ms and 1800 projections were taken around 360°. An isotropic voxel resolution of 10 μm was selected. Object shifting correction and beam hardening correction were applied to the tomographic reconstructions of the acquisitions (NRecon software, Bruker, Kontich, Belgium).

#### 2.6.2. Image analysis

The segmentation and image analysis were based on a previous work where the process is reported in detail [38]. Briefly, the segmentation was performed by using a gaussian mixture model to cluster pixels according to scaffold, bone or soft tissue. Afterward, 3D reconstructions of the segmented data were rendered through a multiplanar reconstruction software (CTVox, Bruker, Kontich, Belgium). Then, for each sample, the percentage of newly formed bone normalized per volume available in the scaffold pores was calculated as the proportion of pixels labeled as bone over the sum of pixels corresponding to soft tissue and new bone and represented with a scatterplot of individual observations overlaid to a boxplot. Subsequently, the radial bone intrusion curves indicating the average bone fraction depending on the radial position were calculated for each individual sample. The combination of trendlines was represented with an average curve and a 95% confidence intervals (CI) region. Finally, the bone distribution axial colormaps representing the average bone fraction among all the samples of each condition depending on the position in the axial projection view were plotted. This analysis was complemented by calculating the percentage of biomaterial surface covered by newly formed bone and the bone growth on the surface of the strands as a function of the offset distance.

The percentage of biomaterial surface covered by newly formed bone was calculated for each scaffold by dividing the surface of the scaffold covered by bone over the total surface of biomaterial available. The surface of biomaterial was determined from the segmented stacks by subtracting to the biomaterial region the same region with one-pixel erosion. This way, a one-pixel thickness layer corresponding to the surface of the biomaterial was obtained. The bone surface in contact with the biomaterial was calculated by performing a conjunction (*i.e.*, AND) Boolean operation to the combination of the one-pixel dilated biomaterial region and the bone region. The result consisted of a one-pixel thickness layer corresponding to the interface between regions. It was assumed that the number of pixels of these two calculated regions was directly proportional to the surfaces available (as the pixels are isotropic). The individual observations of the percentage of biomaterial surface covered by newly formed bone were plotted as a scatterplot and grouped in a boxplot.

The percentage of bone growth on the surface of the strands as a function of the offset distance was calculated for each scaffold by defining successive 10-micron thick regions covering the biomaterial surface and calculating the percentage of bone over total volume in each of these regions. Then, the trend line of this percentage as a function of the distance from the biomaterial surface was calculated. For each condition, the average trend lines and 95% CI regions were plotted.

A detailed description of the image analysis workflow is provided in the supporting information section. The implementation codes in Python (Python 3.9.0, www.python.org) are available in the Git repository https://github.com/YAGORAYMOND/uCT-image-analysis.

### 2.7. Histological assessment

After μ-CT analysis, the dehydrated samples were successively immersed in ethanol solutions with increasing concentrations (*i.e.*, 25, 50, 75, and 100 wt%) of methyl methacrylate resin (Technovit 7200 VLC, Germany). The final resin embedding was held under vacuum overnight and photopolymerized in a UV lamp (EXAKT 520, Exakt Technologies, Germany). Subsequently, the polymerized samples were cut with a diamond band saw (EXAKT 300 CP, Exakt Technologies, Germany) through the central longitudinal cross-section of the scaffold. One half was polished (P4000 grain, Surface grinder, EXAKT 400 CS, AW110, Exakt Technologies, Germany), sputter-coated with carbon, and observed through SEM (Phenom XL, Phenom world, Thermo Fischer Scientific, MA, USA) using a beam accelerating voltage of 10 kV and a secondary electron detector. The mapping scan utility (Automated image mapping software, Phenom ProSuite, Pehnom World, Thermo Fischer Scientific, MA, USA) was used to acquire images of the complete cross-sections. A 300 μm-thick slice was cut from the other half sample, polished down to 30–50 μm, and stained with Masson-Goldner trichrome for histological observation under bright-field microscopy (BX51-P, Olympus, Japan).

### 2.8. Statistical analysis

The scaffold's ultimate compressive strength is presented in a bar chart as mean values ± standard deviation. The μ-CT quantifications percentages of bone volume and biomaterial surface covered by bone are presented as boxplots (indicating the median and quartiles) with overlaid dots representing the individual observations. Statistically significant differences between specimens were calculated (Minitab®19, MiniTab Inc., PA, USA) by one-way analysis of variance (ANOVA) combined with Tukey's *post hoc* test. The confidence interval was set to 95% ($\alpha = 0.05$) for all the analyses.

## 3. Results

### 3.1. Material characterization

C- and S-scaffolds were printed using a self-setting ink that hardens as a result of the hydrolysis of α-TCP to CDHA. The XRD analysis revealed the same phase composition irrespective of the geometry of the filaments of the scaffolds (Fig. 1-I). Rietveld quantification of the crystalline phases using an external standard revealed a composition of 78.8% CDHA, 10.1% β-tricalcium phosphate (β-TCP), and 11.2% amorphous phase. No unreacted α-TCP was detected in any of the samples.

The FTIR spectra (Fig. 1-II) showed the same absorption bands for both conditions, which correspond to the different vibration modes of $PO_4^{3-}$ (*i.e.*, $\nu1 \approx 980$, $\nu2 \approx 363$, $\nu3 \approx 1082$ and $\nu4 \approx 515$ $cm^{-1}$) [39] characteristic of the calcium phosphates. Moreover, the absorption bands of $HPO_4^{2-}$ (*i.e.*, $\approx 870$ $cm^{-1}$) and $OH^-$ (*i.e.*, $\approx 631$ and 3570 $cm^{-1}$), characteristic of calcium-deficient hydroxyapatite [40], were identified in both samples. Additionally, the $H_2O$ stretching and bending bands corresponding to the humidity absorbed by the samples can be noticed at wavelengths of 3500 and 1500 $cm^{-1}$, respectively.

Images of the 3D-printed scaffold architectures with cylindrical and star-shaped strands, obtained by μ-CT are shown in Fig. 1-III. These 3D stacks revealed that there was an appropriate contact between successive layers and that all filaments were well seated in the anterior layer in each of the crossover regions, even with the star-shaped strands. However, it was noticed that for the S-scaffolds some strands presented a twisting and were not contacting the adjacent layer on the two edges of the star cross-section but only on a single edge. This event was further corroborated in later cross-sectional observations (Figs. 2-III, 3-VII and X). SEM observations revealed that both samples had the same microstructure, consisting of an entangled network of acicular crystals, larger on the external surface of the filaments and smaller in the interior (Fig. 1-IV) and, as expected, had very similar specific surface area as determined by nitrogen adsorption (Table 1).

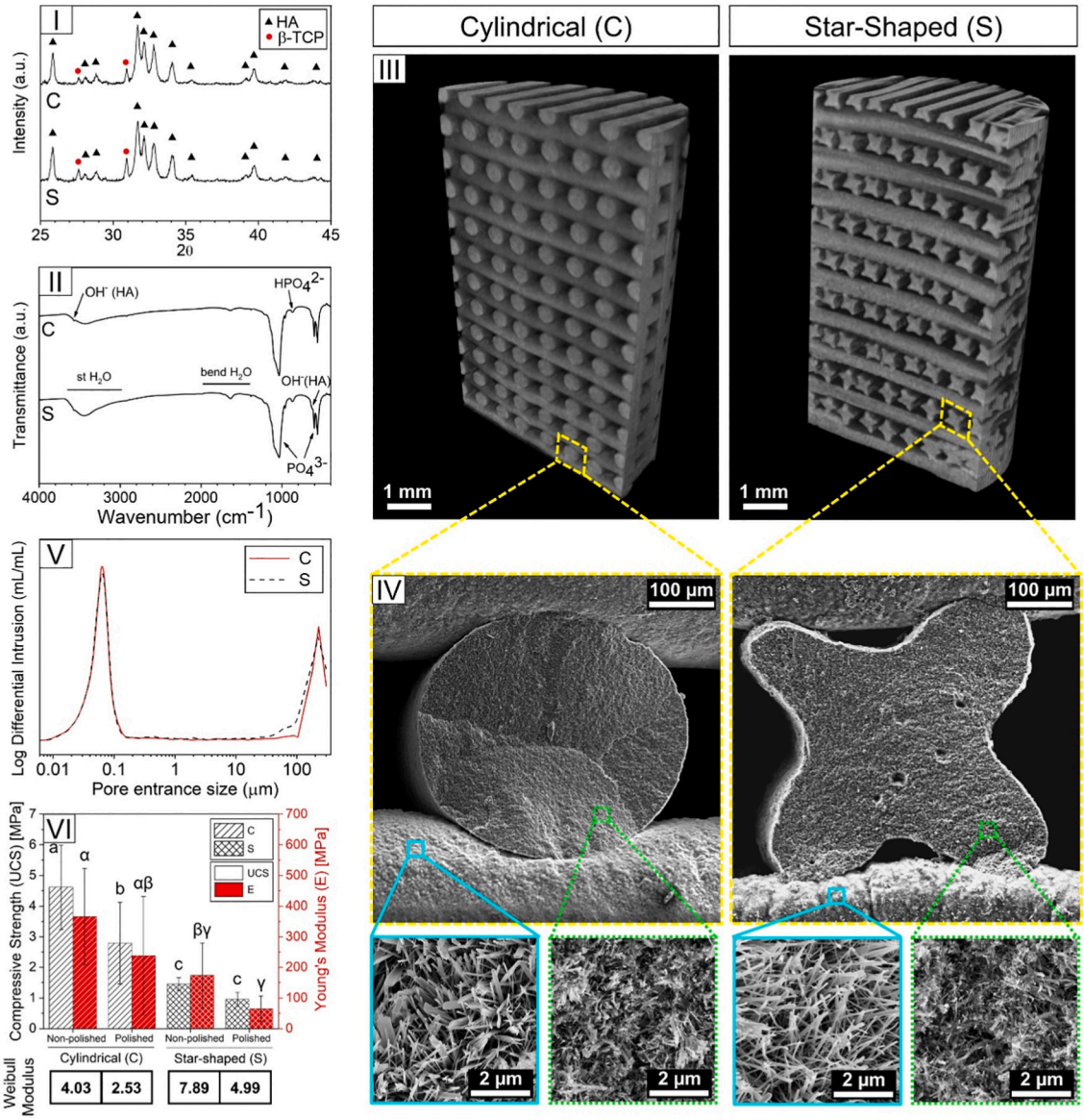


**Fig. 1.** (I) XRD patterns; (II) FTIR spectra; (III) Scaffold morphology obtained by μ-CT; (IV) scaffold microstructure observed by SEM; (V) Pore entrance size distribution as measured by MIP; (VI) Ultimate compressive strength (UCS), Young's modulus (E) and Weibull statistical distribution of strength, of the cylindrical and star-shaped-strand samples. Statistically significant differences in UCS and E are indicated with different Latin and Greek letters, respectively ($p < 0.05$).

The textural properties of the two scaffold types are displayed in Table 1. The macroporosity obtained in the 3D-printed structures during the printing process was quantified by μ-CT, obtaining values of 41.08 ± 1.50% and 48.38 ± 1.36% for the C- and S-scaffolds, respectively. The closed porosity represented less than 1% for both conditions. μ-CT also allowed to calculate the envelope specific surface area of the strands, which as expected was larger for the S- than for the C-scaffolds. When normalizing the material surface (MS) both per volume of material (MS/MV) and per strut length (MS/strand mm), the value was twice as high for the S-scaffolds as for the control.

The pore entrance size distribution of the two scaffolds obtained by MIP (Fig. 1-V) showed a similar bimodal porosity distribution, irrespective of the strand section geometry. The two pore entrance size levels correspond to the intrastrand and the interstrand porosity. For both sample types, the intrastrand porosity was in the range of 0.01 to 0.2 μm and the interstrand porosity was in the size range of 100 to 360 μm, where the larger threshold corresponds to the upper limit of detection of this technique. The total porosity measured by gravimetric methods was 75.78 and 78.72% for the C- and S-scaffolds, respectively. The intrastrand microporosity, assessed from the MIP results, was similar for both sample types, and the same stands for the specific surface area measured by nitrogen adsorption.

The C-scaffolds had a significantly higher compressive strength, as shown in Fig. 1-VI, with 4.61 ± 1.38 MPa and 2.79 ± 1.34 MPa for the non-polished and polished specimens, respectively, compared to the S-scaffolds that resulted in 1.45 ± 0.21 MPa and 0.96 ± 0.23 MPa, respectively. Furthermore, a higher elastic modulus was also found in the C-scaffolds, with 366 ± 157 MPa and 238 ± 193 MPa for the non-polished and polished specimens, respectively, in comparison to the 174 ± 106 MPa and 65 ± 42 MPa observed in the S-scaffolds, for the two same polishing conditions. Moreover, a larger Weibull modulus was found in S-scaffolds, indicating a more homogeneous flaw distribution and thus lower variability in the strength values. In both scaffold types, the grinding resulted in a reduction of the compressive strength and Weibull modulus.

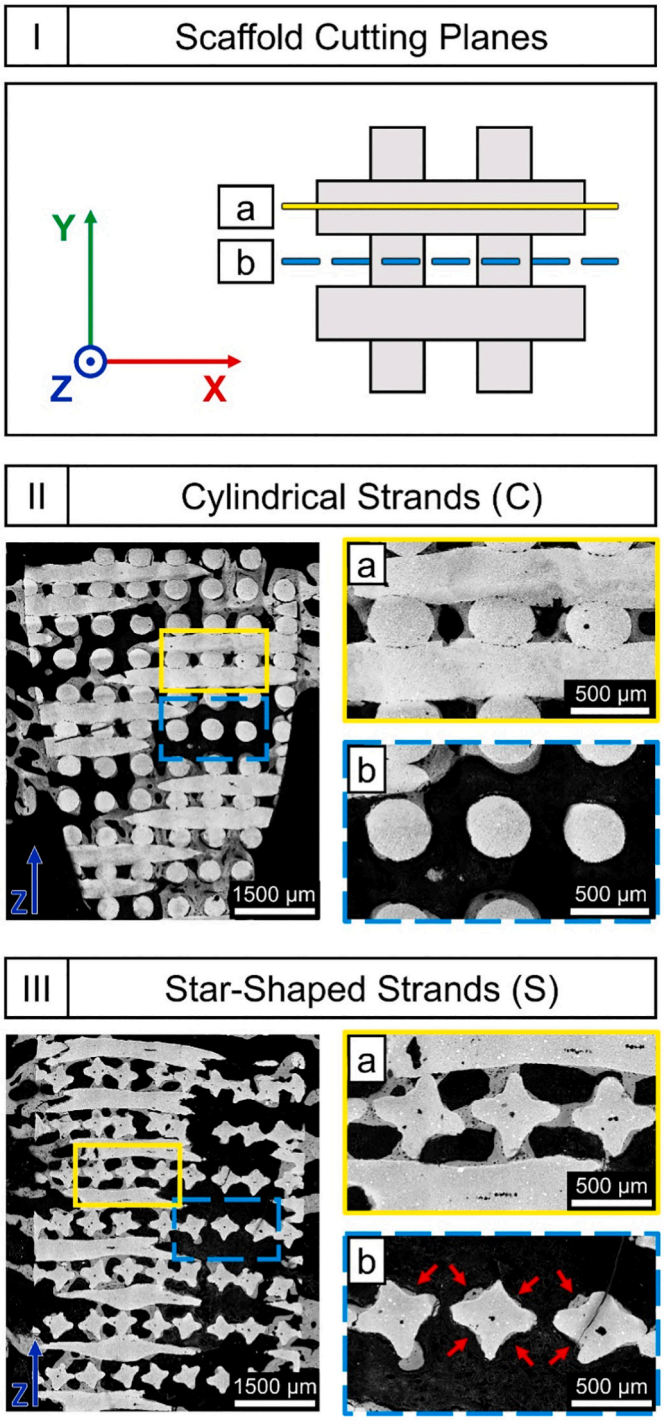


**Fig. 2.** (I) Schema illustrating the two cutting-planes observed in the histological cross-sections: (a) plane cutting the center of the strand intersections, and (b) plane cutting the center of the Z-direction pores. (II and III) SEM images of the histological axial cross-section cuts for the cylindrical-stranded scaffolds and star-shape-stranded scaffolds, respectively, where the (a) and (b) regions can be identified. Red arrows indicate the bone ingrowth on the concave strand surfaces in these second regions.

### 3.2. *In vivo study*

All the animals completed the postoperative period with no clinical complications, weight loss, behavior changes, or lameness. No signs of wound infection, wound dehiscence, or implant migration were observed. During the explantation and soft tissue removal process, one sample (belonging to the S group) was damaged and dismissed from the study.

Bone was found in direct contact with the scaffolds and no immune rejection was observed, indicating the good biocompatibility of the material. Histological analysis was used to assess the bone morphology and degree of maturity and distribution. Additionally, µ-CT was used to quantify in three dimensions the amount of newly formed bone and identify the degree of penetration into the scaffolds.

#### 3.2.1. *Microscopic assessment of the bone formation*

SEM micrographs of the resin-embedded scaffold cross-sections (Fig. 2-I) showed the scaffold porous structure (in light grey) surrounded by newly formed bone (dark grey) in direct contact with the biomaterial. Due to limitations in the precision of the resin-embedded-sample-cutting technique, the axes of the cross-sectional cuts were not perfectly aligned to the printing axis. This is a common occurrence when performing histological cuts of robocasted samples [29,41]. A positive consequence is that this allowed observing two regions of the scaffold in the same sample cut: the plane cutting the center of the strand intersection pillars (Fig. 2-I(a)) and the plane cutting the center of the Z-direction pores (Fig. 2-I(b)). On the one hand, the region of strand intersections presented a similar bone distribution in both sample types, with newly formed bone growing on the concave surfaces formed by the strand intersections, linking the different strands (Fig. 2-II(a) and III(a)). On the other hand, in the second region, bone was preferentially found in the star-shaped strands, deposited at the concave regions originated by its star-shaped geometry (Fig. 2-III(b)).

The histological assessment (Fig. 3) evidenced a high biocompatibility for both sample types, with a high degree of osseointegration and a proper osteoconduction throughout all the scaffolds. No signs of bone necrosis, inflammation areas nor scaffold encapsulation were observed in any sample. Tissular continuity was found in both conditions (Fig. 3-I, IV, VII, and X). A close-up look at the histological slides revealed the presence of a broad network of vascular canals in the macropores of both sample types (Fig. 3-VI, IX, and XII). No differences in terms of bone structure and morphology were observed between sample conditions with this technique. Moving on to detailed observations of the higher magnification images, in Fig. 3-III lamellar bone is observed forming in apposition to preexistent less mature woven bone located in the corner created by the intersection of two strands of consecutive layers. This suggests that the bone formation process has its origin in such regions. In Fig. 3-V a woven bone region is shown with three crossing vascular canals sectioned through the longitudinal axis by the histological section. On the right canal, aligned erythrocytes within a small blood vessel are observed, whereas in the central canal an osteoclast-like multinucleated cell is visible. Such vascularization favors the deposition of lamellar bone around the vascular canals indicating an active remodeling process. Similar dispositions are found for the S condition in Fig. 3-IX, where a blood vessel inside the vascular canal is discerned. In this case, the structure surrounding the Haversian canal is at a more mature stage showing the striated layers of surrounding concentric lamellae. Finally, in Fig. 3-XII the transversal cut of a vascular canal with identifiable erythrocytes inside the vascular structure is visible. Moreover, in the upper left region of the vessel, the diapedesis process of a multinuclear cell is observed, which could be attributed to the initial stage in the formation of a cutting cone.

#### 3.2.2. *µ-CT: 3D reconstruction and morphometric quantification*

3D reconstructions of the segmented µ-CT acquisitions (Fig. 4) allowed to assess the distribution of the newly formed bone within the scaffolds and compare the best and worst cases within each sample condition.

The overall percentage of newly formed bone on available volume was higher for the star-shape-stranded scaffolds (43.60 ± 10.32%) than for the cylindrical-stranded scaffolds (37.34 ± 5.08%), although the difference was not statistically significant (Fig. 5-I). The bone

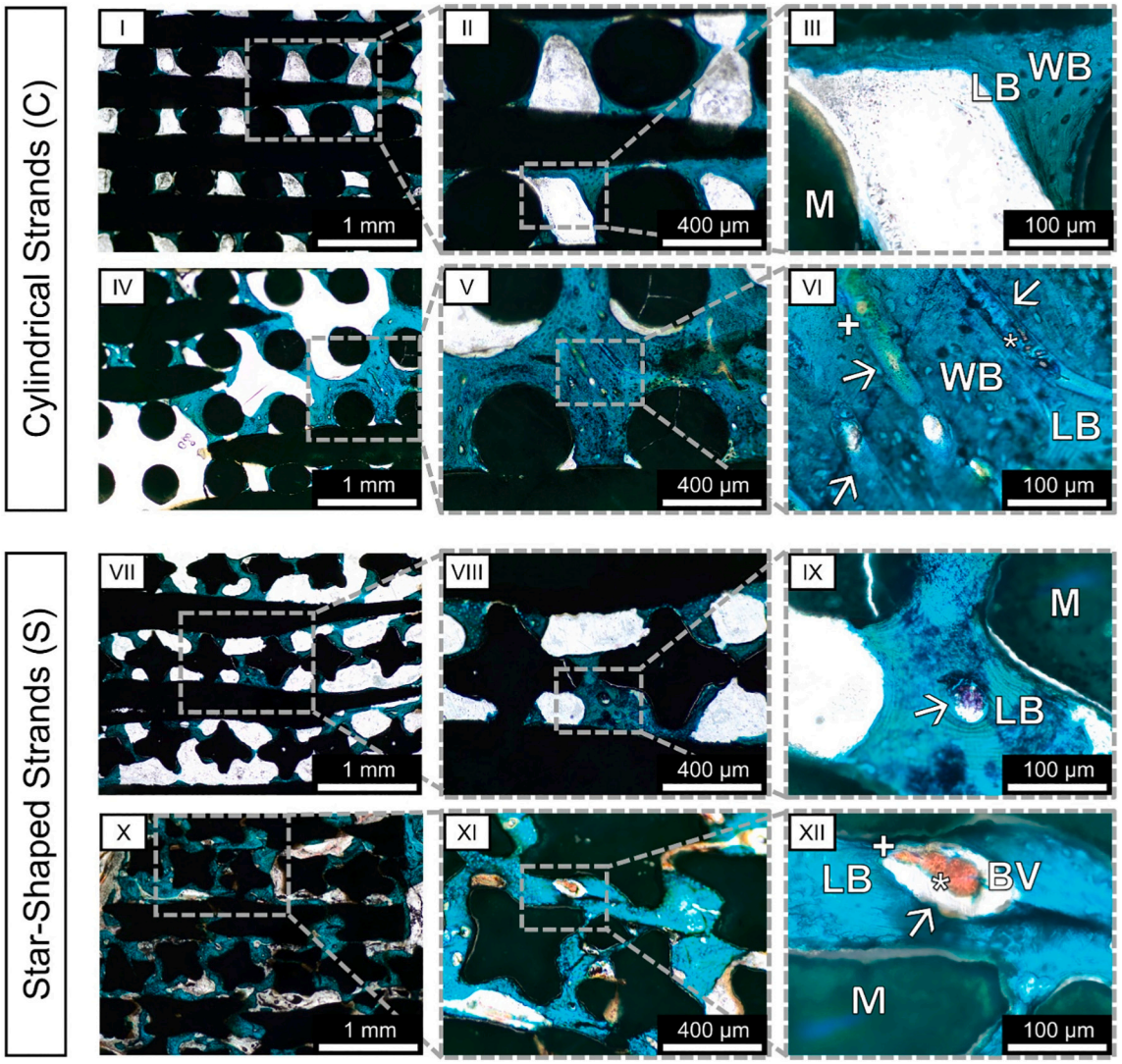


**Fig. 3.** Masson-Goldner trichrome staining of the histological slides of the cylindrical-stranded scaffolds (C) and star-shape-stranded scaffolds (S). Bone appears colored in green-blue and biomaterial in dark. M = biomaterial, WB = woven bone, LB = lamellar bone, (➔) = vascular canal, (*) = erythrocytes, (+) = multi-nucleated cell, BV = blood vessel.

**Table 1**
Density and textural properties of the 3D-printed scaffolds composed of cylindrical and star-shaped strands.

| Properties | Cylindrical* | Star-shaped* |
|---|---|---|
| Skeletal density ($\rho_{skel}$) | 3.06 g cm$^{-3}$ | 3.07 g cm$^{-3}$ |
| Apparent density ($\rho_{app}$) | 0.74 ± 0.03 g cm$^{-3}$(a) | 0.65 ± 0.04 g cm$^{-3}$(b) |
| Total porosity ($P_{tot}$) | 75.78 ± 1.07%(a) | 78.72 ± 1.21%(b) |
| Intrastrand microporosity ($P_{micro}$) | 56.67% | 56.81% |
| Macroporosity ($P_{macro}$) | 41.08 ± 1.50%(a) | 48.38 ± 1.36%(b) |
| Specific surface area ($SSA_{BET}$) | 27.11 m$^2$ g$^{-1}$ | 26.55 m$^2$ g$^{-1}$ |
| Specific surface area (MS/MV) [µ-CT] | 9.06 ± 0.23 mm$^2$ mm$^{-3}$(a) | 20.38 ± 0.38 mm$^2$ mm$^{-3}$(b) |
| Specific surface area (MS/strand mm) [µ-CT] | 1.18 ± 0.03 mm$^2$ strand mm$^{-1}$(a) | 2.04 ± 0.04 mm$^2$ strand mm$^{-1}$(b) |

* (a) and (b) indicate statistically significant differences between conditions ($p < 0.05$).

distribution as a function of the radial distance from the scaffold surface is displayed in Fig. 5-II, which represents the degree of bone intrusion for both samples. Additionally, the degree of bone intrusion can also be shown by mapping the overall average bone percentage in a cumulated projection of the scaffold's axial cross-section, as displayed in Fig. 5-III. The colormap ranges from blue to red corresponding to 0 and 100% of newly formed bone in available volume, respectively. The percentage of biomaterial surface covered by newly formed bone was also quantified, obtaining a 57.82 ± 11.28% and 65.11 ± 11.72% for the C and S scaffolds, respectively (Fig. 5-IV), although the difference was not statistically significant. Finally, the thickness of the bone grown on the surface of the strands with different geometries was quantified by determining the percentage of bone on available volume at different offset radial distances from the strand surface. The results are shown in Fig. 5-V with trendlines and 95% CI of the estimate.

## 4. Discussion

Surface curvature has been highlighted as a decisive parameter in tissue growth [24,25], and more specifically in bone formation [20,28]. Therefore, it should be taken into account as a design criterion for bone scaffolds. Some methods of manufacturing macroporous scaffolds, such as foaming or particle leaching, directly result in structures with predominating concave surfaces. This is not the case for microextrusion-based techniques, which typically use circular nozzles and therefore result in porous structures with predominating convex surfaces.

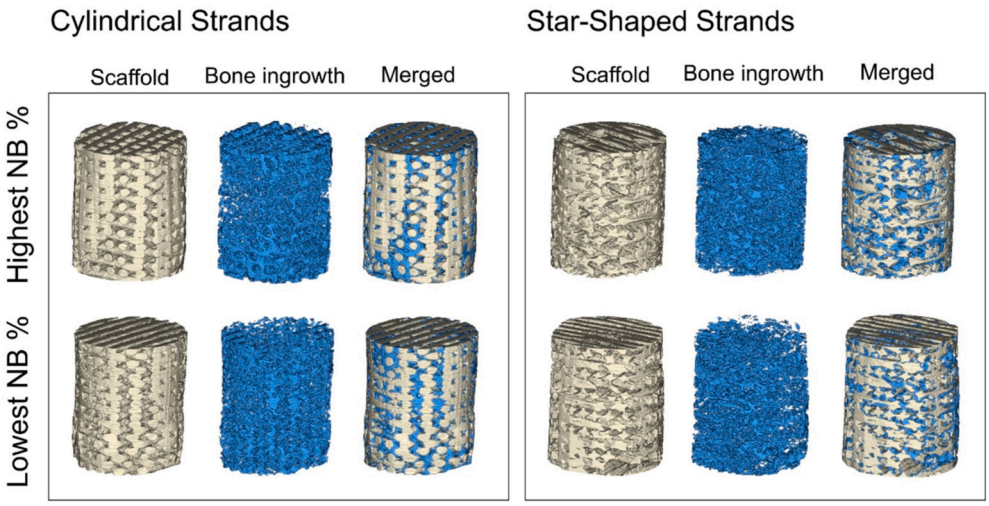


**Fig. 4.** Representative μ-CT reconstructions of the samples with highest and lowest percentage of newly formed bone (NB %) for the scaffolds printed with cylindrical (left) and star-shaped (right) strands.

However, modification of the nozzle cross-section also allows the printing of non-cylindrical filaments with concave surfaces, introducing an additional degree of control to the pore geometry by this technique [35]. In this study, we analyzed the impact of strand surface curvature of 3D-printed calcium phosphate scaffolds on the bone regeneration capacity in a rabbit model.

As shown by XRD and FTIR, (Fig. 1-I and II) the two scaffold types, with different strand geometries, *i.e.*, cylindrical *vs.* star-shaped, had the same composition, consisting mostly of CDHA with a small amount of β-TCP, as a result of the hydrothermal transformation of α-TCP [33,38]. FTIR confirmed the calcium-deficient nature of the HA, associated with the hydrolysis-based hardening reaction process [42]. SEM observations revealed similar microstructures for both scaffolds, consisting of an entangled network of acicular crystals characteristic of the HA obtained by hydrothermal processes [43]. Consequently, the SSA measured by nitrogen adsorption was almost identical for both scaffolds. However, clear differences in crystal length were observed when comparing the internal and external microstructures in both scaffold types. This can be attributed to the available space for crystal growth at the surface, leading to longer needles.

Although the printing parameters were adjusted to obtain macropores as similar as possible for the two groups by imposing the same infill percentage, the different strand morphology and different layer height, that had to be optimized for each stand morphology, resulted in a difference in macroporosity of 7.3% (Table 1). This represents a relative increase of macroporosity for the S-scaffolds of 17.8%, which has to be taken into account, together with other geometrical aspects, when analyzing the *in vivo* performance of this group. On the other hand, the intrastrand microporosity percentage (Table 1) and the micro- and macropore size ranges (Fig. 1-V) were very similar in both groups.

Regarding the regularity of the 3D-printed structures and the disposition of the strands, adequate global cohesion between successive layers was observed in the structures for both types of filaments. Due to gravity, the deposited ink flows downwards until it rests on the previous layer, enabling good contact between filaments. However, in star-shaped filaments, due to the characteristic geometry, four contact zones are established at each strand crossing point, with a much smaller total contact surface than in the case of cylindrical filaments. This makes it much more unlikely to capture these contact zones in the sections observed by SEM or optical microscopy (*i.e.*, Figs. 2-III and 3). Moreover, it was observed that in the S-scaffolds some strands appeared twisted at some regions. This can be attributed to torsional forces associated to the change of strand deposition direction, a phenomenon that was extensively discussed and characterized in a previous work [35]. It may take some distance for the strand to return to the stable position and, in the transition region the strands appear twisted. While this phenomenon has no visible repercussion for the cylindrical strands, which have a geometry invariant to axial torsion, in the star-shaped group this may lead to variation in layer height or to a reduced contact between successive layers or impaired connections between crossing strands (Fig. 2-III(a)).

These reduced contact regions and impaired or absent connections in some cases also had a detrimental impact on the mechanical performance. Hence, the strands with a fluted morphology presented a reduced compressive strength and elastic modulus (Fig. 1-VI). The relation of the smaller contact surface between successive layers characteristic of the S-scaffolds, resulting in higher stress concentrations, was already reported in a previous study [35].

Concerning the mechanical properties, it was also observed that grinding reduced both the scaffold's compressive strength and Young's modulus. This behavior can be explained by the removal of the external layer of the scaffold, which has a lower porosity due to the bending of the strands when changing the printing direction.

As expected, bone grew throughout the porous structure in the two scaffold architectures (Fig. 4) as the scaffold material, a biomimetic calcium-deficient hydroxyapatite, is known to be highly osteoconductive [44]. Moreover, the interconnected porosity of the 3D architecture led to a widespread vessel network, resulting in a highly vascularized tissue, as observed in the histological slides stained with Masson-Goldner trichrome (Fig. 3).

Although the differences found in the histomorphometric quantification were not statistically significant, all the results showed a clear trend indicating that the strands with added concavities had a favorable effect in the amount of newly formed bone, the degree of bone penetration into the structure, and the thickness of the layer of bone formed on the strands. The μ-CT histomorphometric analysis allowed not only to quantify the amount of newly formed bone in three dimensions but also to determine its spatial distribution. A larger amount of regenerated bone was found when the scaffolds were printed with fluted star-shaped strands, although the increase was not statistically significant (Fig. 5-I). This is in agreement with previous studies reporting that the bone formation rate is accelerated on surfaces with smaller concave curvature radii [24,25,27]. Furthermore, the S-scaffolds showed better osteoconductive properties, leading to a higher degree of bone intrusion towards the core of the structure, as shown in the radial bone intrusion trendlines of Fig. 5-II and in the average bone percentage mappings of Fig. 5-III. Whereas both scaffold types presented an initial exponential decrease of the bone percentage in the first 0.5 mm perimetral region, the amount of bone was constant from this point for the S-scaffolds,

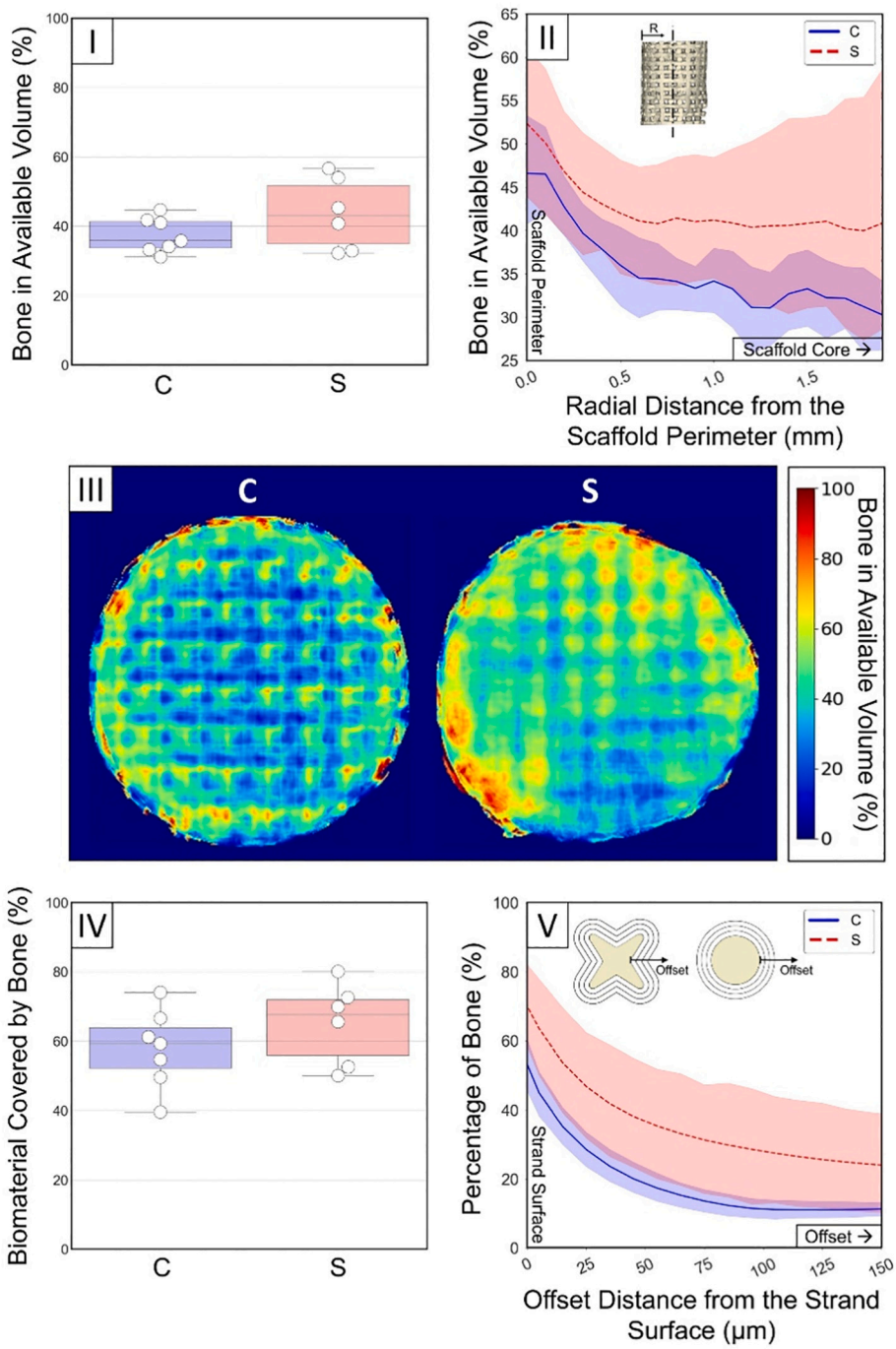


**Fig. 5.** (I) Quantification of the percentage of newly formed bone in the available volume; (II) radial bone intrusion into the scaffold. The solid and dashed lines represent the average value and the surrounding transparency-colored regions represent the 95% CI for that estimate; (III) cumulate mapping of the percentage of newly formed bone in available volume; (IV) percentage of biomaterial surface covered by newly formed bone and (V) bone growth on the surface of the cylindrical (C) and star-shaped (S) strands. No statistically significant differences were found in sections I and IV ($p < 0.05$).

while for the C-scaffolds it followed a decreasing trend towards the center. Furthermore, the vertical offset also indicated a global larger amount of bone formation in S-scaffolds with regard to C-scaffolds.

Consistent with these results, the mappings of bone percentage showed the highest amounts of bone in the perimetral areas of the scaffold. Moreover, the S samples presented a higher percentage of bone than the C samples, and these differences became more remarkable in the core of the scaffolds, suggesting a higher level of osteoconduction for the S samples. The architecture of both scaffolds was clearly identified in the mapping since in all the samples the orthogonal pattern was aligned. This was confirmed by the quantification of the surface of the strands covered by newly formed bone (Fig. 5-IV), resulting in higher values for the scaffolds with star-shaped strands compared to the cylindrical ones.

Different factors may contribute to the star-shaped strand scaffolds favouring bone colonization. While strand curvature might be one of the relevant factors, other elements associated to the geometrical specificities of each group may also play a role. For instance, the higher macroporosity of the star-shaped strand scaffolds (*i.e.*, 17.8% in relative values), or the presence of additional gaps or concavities created at strand intersections caused by strand twisting may also contribute to the differences in bone formation. The variation of these geometrical parameters can in turn affect the fluid flow in the two scaffold architectures. Previous studies have shown that pore geometry of bone scaffolds has a strong influence on the permeability and velocity of the fluid flow, which is directly related to the supply and accumulation of oxygen and nutrients at the pore network [45–47]. This is crucial for cell growth and has a straight impact on new bone formation. Hence, while both scaffold types have an open interconnected pore network, the more tortuous

path associated to S as compared to C scaffolds is expected to result in lower internal flow rates at the surface of the strands, which in turn may have an impact on the concentration of soluble species (both ions and growth factors) [47].

Regarding the possible role of the presence of concave channels in the strands of the S-scaffolds, previous studies have reported a positive effect of grooves patterned on metallic surfaces, enhancing and guiding bone formation [48,49] and improving osteoconductive properties [50]. The focus of these works was on guiding bone through the external surface of dental implants to maximize the degree of osseointegration and implant stability. In contrast, the current study harnessed this strategy to enhance bone ingrowth in a calcium phosphate scaffold. As this is a bioactive substrate, in addition to the purely geometrical effect, the impact of the geometry of the surface on the distribution of the ions exchanged with the surrounding fluids, with a possible confinement in the concavities, must be taken into account.

Moreover, the percentage of newly formed bone was calculated as a function of the offset distance from the strand surface (Fig. 5-V). Regardless of the strand geometry, bone started growing on the surface of the scaffold and progressively moved to the center of the pore. This resulted in exponential decay trend lines for both samples, although there was an offset of about 10–15% for the S scaffolds, which showed also a higher variability. This is consistent with the higher amount of bone for the S scaffolds in Fig. 5-I, II, and III. Furthermore, it is worth mentioning that the percentage of bone at $z = 0$ in Fig. 5-V matched the results of Fig. 5-IV, the slight differences being attributed to the different quantification strategies employed. All together validates both quantification analyses.

In the same line, the SEM micrographs (Fig. 2) and histological observations (Fig. 3) revealed a double role of the filament concavities. In the first place, the acceleration of the bone formation process and, in the second place, an enhanced bone guiding function. Regarding the first one, the strand crossing regions presented the majority of the formed bone. This finding is in agreement with previous research that also found the bone starting to grow in more confined regions, such as concavities or corners [20,21,28]. Additionally, it was observed when comparing Fig. 2-II(b) to Fig. 2-III(b) that the strand fluting of the S condition guided the bone growth through regions of the scaffolds that were hardly reached with the traditional strand configuration (*i.e.*, the regions of the cantilever strands connecting the pillars).

The results shown in the present study demonstrate that the filaments with concavities were more efficient in terms of guiding bone formation, and hence, enhancing the global osteoconductive properties of the structure.

However, in fact, no significant increase in bone formation was observed, and the enhancement with respect to scaffolds with cylindrical struts was less remarkable than that obtained with a foamed architecture [28,29]. This can be explained by the fact that, despite having concave surfaces, pore interconnections in the S-scaffolds were very large, and hence they lacked confined microenvironments like those found in foams with bottle-neck interconnections. Therefore, although the physical or mechanical factors associated with curvature-driven tissue formation [25] were indeed present, the chemical effects associated with the retention of soluble proteins and ions might be mitigated by the open nature of the macropore structure and the lack of confined volumes.

## 5. Conclusion

Controlling the morphology of the strands is a promising strategy to enhance bone regeneration on 3D-printed scaffolds. Strands with a fluted morphology appear to be capable of guiding bone faster through the core of the scaffolds than the traditional cylindrical morphologies and, although the differences were not statistically significant, a tendency to promote bone formation was observed. This represents an enhancement of the scaffold's osteogenic and osteoconductive properties. Although this work is a first step that proves the effectiveness of this approach for bone regeneration, further research is needed to fully understand the role of strand geometry (testing multiple geometries and implantation times) and the interaction with the strand printing arrangement (using additional patterns to the orthogonal one). The configuration should be optimized to obtain similar conditions to bottle-neck pores and confined environments in order to turn the 3D-printed morphologies more efficient for bone regeneration.

## CRediT authorship contribution statement

Yago Raymond: Conceptualization, investigation, formal analysis, data curation, writing - original draft preparation; Cyril Lehmann: Investigation; Emilie Thorel: Investigation; Raúl Benitez: Methodology, formal analysis; Antonio Riveiro: Methodology, investigation; Juan Pou: Methodology, investigation; Maria-Cristina Manzanares: Formal analysis; Jordi Franch: Conceptualization, investigation; Cristina Canal: Funding acquisition, reviewing and editing; Maria-Pau Ginebra: Conceptualization, writing- reviewing and editing, supervision, funding acquisition.

## Declaration of competing interest

The authors declare the following financial interests/personal relationships which may be considered as potential competing interests:

MPG has an equity interest in Mimetis Biomaterials, S.L., a spin-off company of UPC that may potentially benefit from the research results displayed in the present work. YR and ET are employees of the same company.

## Acknowledgements

The authors kindly acknowledge the Spanish Ministry of Science, Innovation and Universities for financial support through the PID2019-103892RB-I00/AEI/10.13039/501100011033 project. They also thank the Generalitat de Catalunya for funding through projects 2017SGR-1165 and BASE3D 001-P-001646 co-funded by European Regional Development Funds. YR acknowledges the Spanish Government for the Ph.D. grant DI-15-08184. MPG and CC acknowledge the Generalitat de Catalunya for the ICREA Academia Award. The authors are grateful to Prof. Jordi Franch's team (Veterinary Faculty, UAB) for their valuable collaboration during the surgeries. The authors are also thankful to Dr. Araceli Aznar for her technical assistance with the μ-CT.

## Appendix A. Supplementary data

Supplementary data to this article can be found online at https://doi.org/10.1016/j.bioadv.2022.212807.

## References

[1] M. Javaid, A. Haleem, Additive manufacturing applications in orthopaedics: a review, J. Clin. Orthop. Trauma. 9 (2018) 202–206, https://doi.org/10.1016/j.jcot.2018.04.008.

[2] W. Habraken, P. Habibovic, M. Epple, M. Bohner, Calcium phosphates in biomedical applications: materials for the future? Mater. Today 19 (2016) 69–87, https://doi.org/10.1016/j.mattod.2015.10.008.

[3] M.-P. Ginebra, M. Espanol, Y. Maazouz, V. Bergez, D. Pastorino, Bioceramics and bone healing, EFORT Open Rev. 3 (2018) 173–183, https://doi.org/10.1302/2058-5241.3.170056.

[4] R. Trombetta, J.A. Inzana, E.M. Schwarz, S.L. Kates, H.A. Awad, 3D printing of calcium phosphate ceramics for bone tissue engineering and drug delivery, Ann. Biomed. Eng. 45 (2017) 23–44, https://doi.org/10.1007/s10439-016-1678-3.

[5] J.A. Lewis, G.M. Gratson, Direct writing in three dimensions, Mater. Today 7 (2004) 32–39, https://doi.org/10.1016/S1369-7021(04)00344-X.

[6] E. Feilden, E.G.-T. Blanca, F. Giuliani, E. Saiz, L. Vandeperre, Robocasting of structural ceramic parts with hydrogel inks, J. Eur. Ceram. Soc. 36 (2016) 2525–2533, https://doi.org/10.1016/j.jeurceramsoc.2016.03.001.

[7] A. Lode, K. Meissner, Y. Luo, F. Sonntag, S. Glorius, B. Nies, C. Vater, F. Despang, T. Hanke, M. Gelinsky, Fabrication of porous scaffolds by three-dimensional

plotting of a pasty calcium phosphate bone cement under mild conditions, J. Tissue Eng. Regen. Med. 8 (2014) 682–693, https://doi.org/10.1002/term.1563.
[8] Y. Maazouz, E.B. Montufar, J. Guillem-Marti, I. Fleps, C. Öhman, C. Persson, M. P. Ginebra, Robocasting of biomimetic hydroxyapatite scaffolds using self-setting inks, J. Mater. Chem. B 2 (2014) 5378–5386, https://doi.org/10.1039/C4TB00438H.
[9] N. Raja, H. Yun, A simultaneous 3D printing process for the fabrication of bioceramic and cell-laden hydrogel core/shell scaffolds with potential application in bone tissue regeneration, J. Mater. Chem. B 4 (2016) 4707–4716, https://doi.org/10.1039/C6TB00849F.
[10] T. Ahlfeld, A.R. Akkineni, Y. Förster, T. Köhler, S. Knaack, M. Gelinsky, A. Lode, Design and fabrication of complex scaffolds for bone defect healing: combined 3D plotting of a calcium phosphate cement and a growth factor-loaded hydrogel, Ann. Biomed. Eng. 45 (2017) 224–236, https://doi.org/10.1007/s10439-016-1685-4.
[11] M.C. von Doernberg, B. von Rechenberg, M. Bohner, S. Grünenfelder, G.H. van Lenthe, R. Müller, B. Gasser, R. Mathys, G. Baroud, J. Auer, In vivo behavior of calcium phosphate scaffolds with four different pore sizes, Biomaterials 27 (2006) 5186–5198.
[12] H. Lapczyna, L. Galea, S. Wüst, M. Bohner, S. Jerban, A. Sweedy, N. Doebelin, N. van Garderen, S. Hofmann, G. Baroud, R. Müller, B. von Rechenberg, Effect of grain size and microporosity on the in vivo behaviour of β-tricalcium phosphate scaffolds, Eur. Cells Mater. 28 (2014) 299–319, https://doi.org/10.22203/eCM.v028a21.
[13] C. Ghayor, F.E. Weber, Osteoconductive microarchitecture of bone substitutes for bone regeneration revisited, Front. Physiol. 9 (2018) 1–10, https://doi.org/10.3389/fphys.2018.00960.
[14] V.P. Galván-Chacón, P. Habibovic, Deconvoluting the bioactivity of calcium phosphate-based bone graft substitutes: strategies to understand the role of individual material properties, Adv. Healthc. Mater. 6 (2017) 1601478, https://doi.org/10.1002/adhm.201601478.
[15] V. Karageorgiou, D. Kaplan, Porosity of 3D biomaterial scaffolds and osteogenesis, Biomaterials 26 (2005) 5474–5491, https://doi.org/10.1016/j.biomaterials.2005.02.002.
[16] A. Kumar, S. Mandal, S. Barui, R. Vasireddi, U. Gbureck, M. Gelinsky, B. Basu, Low temperature additive manufacturing of three dimensional scaffolds for bone-tissue engineering applications: processing related challenges and property assessment, Mater. Sci. Eng. R Rep. 103 (2016) 1–39, https://doi.org/10.1016/j.mser.2016.01.001.
[17] O. Chan, M.J. Coathup, A. Nesbitt, C.-Y. Ho, K.A. Hing, T. Buckland, C. Campion, G.W. Blunn, The effects of microporosity on osteoinduction of calcium phosphate bone graft substitute biomaterials, Acta Biomater. 8 (2012) 2788–2794, https://doi.org/10.1016/j.actbio.2012.03.038.
[18] M.J. Coathup, K.A. Hing, S. Samizadeh, O. Chan, Y.S. Fang, C. Campion, T. Buckland, G.W. Blunn, Effect of increased strut porosity of calcium phosphate bone graft substitute biomaterials on osteoinduction, J. Biomed. Mater. Res. Part A. 100A (2012) 1550–1555, https://doi.org/10.1002/jbm.a.34094.
[19] S. Ehrig, B. Schamberger, C.M. Bidan, A. West, C. Jacobi, K. Lam, P. Kollmannsberger, A. Petersen, P. Tomancak, K. Kommareddy, F.D. Fischer, P. Fratzl, J.W.C. Dunlop, Surface tension determines tissue shape and growth kinetics, Sci. Adv. 5 (2019) 1–9, https://doi.org/10.1126/sciadv.aav9394.
[20] U. Ripamonti, J. Crooks, A.N. Kirkbride, Sintered porous hydroxyapatites with intrinsic osteoinductive activity: geometric induction of bone formation, S. Afr. J. Sci. 95 (1999) 335–343.
[21] U. Ripamonti, P.W. Richter, M.E. Thomas, Self-inducing shape memory geometric cues embedded within smart hydroxyapatite-based biomimetic matrices, Plast. Reconstr. Surg. 120 (2007) 1796–1807, https://doi.org/10.1097/01.prs.0000287133.43718.89.
[22] G. Daculsi, T. Miramond, P. Borget, S. Baroth, Smart calcium phosphate bioceramic scaffold for bone tissue engineering, Key Eng. Mater. 529–530 (2012) 19–23, https://doi.org/10.4028/www.scientific.net/KEM.529-530.19.
[23] U. Ripamonti, Soluble osteogenic molecular signals and the induction of bone formation, Biomaterials 27 (2006) 807–822, https://doi.org/10.1016/j.biomaterials.2005.09.021.
[24] M. Rumpler, A. Woesz, J.W.C. Dunlop, J.T. van Dongen, P. Fratzl, The effect of geometry on three-dimensional tissue growth, J. R. Soc. Interface 5 (2008) 1173–1180, https://doi.org/10.1098/rsif.2008.0064.
[25] C.M. Nelson, R.P. Jean, J.L. Tan, W.F. Liu, N.J. Sniadecki, A.A. Spector, C.S. Chen, Emergent patterns of growth controlled by multicellular form and mechanics, Proc. Natl. Acad. Sci. 102 (2005) 11594–11599, https://doi.org/10.1073/pnas.0502575102.
[26] C.M. Bidan, K.P. Kommareddy, M. Rumpler, P. Kollmannsberger, Y.J.M. Bréchet, P. Fratzl, J.W.C. Dunlop, How linear tension converts to curvature: geometric control of bone tissue growth, PLoS One 7 (2012), e36336, https://doi.org/10.1371/journal.pone.0036336.
[27] C.M. Bidan, K.P. Kommareddy, M. Rumpler, P. Kollmannsberger, P. Fratzl, J.W. C. Dunlop, Geometry as a factor for tissue growth: towards shape optimization of tissue engineering scaffolds, Adv. Healthc. Mater. 2 (2013) 186–194, https://doi.org/10.1002/adhm.201200159.
[28] A. Barba, A. Diez-Escudero, Y. Maazouz, K. Rappe, M. Espanol, E.B. Montufar, M. Bonany, J.M. Sadowska, J. Guillem-Marti, C. Öhman-Mägi, C. Persson, M.-C. Manzanares, J. Franch, M.-P. Ginebra, Osteoinduction by foamed and 3D-printed calcium phosphate scaffolds: effect of nanostructure and pore architecture, ACS Appl. Mater. Interfaces 9 (2017) 41722–41736, https://doi.org/10.1021/acsami.7b14175.
[29] A. Barba, Y. Maazouz, A. Diez-Escudero, K. Rappe, M. Espanol, E.B. Montufar, C. Öhman-Mägi, C. Persson, P. Fontecha, M.-C. Manzanares, J. Franch, M.-P. Ginebra, Osteogenesis by foamed and 3D-printed nanostructured calcium phosphate scaffolds: effect of pore architecture, Acta Biomater. 79 (2018) 135–147, https://doi.org/10.1016/j.actbio.2018.09.003.
[30] P. Habibovic, H. Yuan, C.M. van der Valk, G. Meijer, C.A. van Blitterswijk, K. de Groot, 3D microenvironment as essential element for osteoinduction by biomaterials, Biomaterials 26 (2005) 3565–3575, https://doi.org/10.1016/j.biomaterials.2004.09.056.
[31] H. Shao, X. Yang, Y. He, J. Fu, L. Liu, L. Ma, L. Zhang, G. Yang, C. Gao, Z. Gou, Bioactive glass-reinforced bioceramic ink writing scaffolds: sintering, microstructure and mechanical behavior, Biofabrication 7 (2015), 035010, https://doi.org/10.1088/1758-5090/7/3/035010.
[32] C. Wu, Y. Luo, G. Cuniberti, Y. Xiao, M. Gelinsky, Three-dimensional printing of hierarchical and tough mesoporous bioactive glass scaffolds with a controllable pore architecture, excellent mechanical strength and mineralization ability, Acta Biomater. 7 (2011) 2644–2650, https://doi.org/10.1016/j.actbio.2011.03.009.
[33] S. Raymond, Y. Maazouz, E.B. Montufar, R.A. Perez, B. González, J. Konka, J. Kaiser, M. Ginebra, Accelerated hardening of nanotextured 3D-plotted self-setting calcium phosphate inks, Acta Biomater. 75 (2018) 451–462, https://doi.org/10.1016/j.actbio.2018.05.042.
[34] L. Vidal, C. Kampleitner, S. Krissian, M.Á. Brennan, O. Hoffmann, Y. Raymond, Y. Maazouz, M.-P. Ginebra, P. Rosset, P. Layrolle, Regeneration of segmental defects in metatarsus of sheep with vascularized and customized 3D-printed calcium phosphate scaffolds, Sci. Rep. 10 (2020) 7068, https://doi.org/10.1038/s41598-020-63742-w.
[35] Y. Raymond, E. Thorel, M. Liversain, A. Riveiro, J. Pou, M.-P. Ginebra, 3D printing non-cylindrical strands: morphological and structural implications, Addit. Manuf. 46 (2021), 102129, https://doi.org/10.1016/j.addma.2021.102129.
[36] D. Pastorino, C. Canal, M.-P. Ginebra, Multiple characterization study on porosity and pore structure of calcium phosphate cements, Acta Biomater. 28 (2015) 205–214, https://doi.org/10.1016/j.actbio.2015.09.017.
[37] N.R. Council, Guide for the Care and Use of Laboratory Animals, National Academies Press, Washington, D.C, 2011, https://doi.org/10.17226/12910.
[38] Y. Raymond, M. Bonany, C. Lehmann, E. Thorel, R. Benítez, J. Franch, M. Espanol, X. Solé-Martí, M.-C. Manzanares, C. Canal, M.-P. Ginebra, Hydrothermal processing of 3D-printed calcium phosphate scaffolds enhances bone formation in vivo: a comparison with biomimetic treatment, Acta Biomater. 135 (2021) 671–688, https://doi.org/10.1016/j.actbio.2021.09.001.
[39] V.M. Bhatnagar, Infrared spectrum of strontium hydroxyapatite, Experientia 23 (1967) 697–699, https://doi.org/10.1007/BF02154118.
[40] M. Mir, F.L. Leite, P.S. de P. Herrmann Junior, F.L. Pissetti, A.M. Rossi, E. L. Moreira, Y.P. Mascarenhas, XRD, AFM, IR and TGA study of nanostructured hydroxyapatite, Mater. Res. 15 (2012) 622–627, https://doi.org/10.1590/S1516-14392012005000069.
[41] P. Diloksumpan, R.V. Bolaños, S. Cokelaere, B. Pouran, J. de Grauw, M. van Rijen, R. van Weeren, R. Levato, J. Malda, Orthotopic bone regeneration within 3D printed bioceramic scaffolds with region-dependent porosity gradients in an equine model, Adv. Healthc. Mater. 1901807 (2020) 1–11, https://doi.org/10.1002/adhm.201901807.
[42] M.P. Ginebra, E. Fernández, E.A.P. De Maeyer, R.M.H. Verbeeck, M.G. Boltong, J. Ginebra, F.C.M. Driessens, J.A. Planell, Setting reaction and hardening of an apatitic calcium phosphate cement, J. Dent. Res. 76 (1997) 905–912, https://doi.org/10.1177/00220345970760041201.
[43] K. Ioku, G. Kawachi, S. Sasaki, H. Fujimori, S. Goto, Hydrothermal preparation of tailored hydroxyapatite, J. Mater. Sci. 41 (2006) 1341–1344, https://doi.org/10.1007/s10853-006-7338-5.
[44] A. Barba, A. Diez-Escudero, M. Espanol, M. Bonany, J.M. Sadowska, J. Guillem-Marti, C. Öhman-Mägi, C. Persson, M.C. Manzanares, J. Franch, M.P. Ginebra, Impact of biomimicry in the Design of Osteoinductive Bone Substitutes: nanoscale matters, ACS Appl. Mater. Interfaces 11 (2019) 8818–8830, https://doi.org/10.1021/acsami.8b20749.
[45] D. Ali, S. Sen, Computational fluid dynamics study of the effects of surface roughness on permeability and fluid flow-Induced Wall shear stress in scaffolds, Ann. Biomed. Eng. 46 (2018) 2023–2035, https://doi.org/10.1007/s10439-018-2101-z.
[46] D. Ali, Effect of scaffold architecture on cell seeding efficiency: a discrete phase model CFD analysis, Comput. Biol. Med. 109 (2019) 62–69, https://doi.org/10.1016/j.compbiomed.2019.04.025.
[47] F. Deng, L. Liu, Z. Li, J. Liu, 3D printed Ti6Al4V bone scaffolds with different pore structure effects on bone ingrowth, J. Biol. Eng. 15 (2021) 4, https://doi.org/10.1186/s13036-021-00255-8.
[48] J. Hall, P. Miranda-Burgos, L. Sennerby, Stimulation of directed bone growth at oxidized titanium implants by macroscopic grooves: an in vivo study, Clin. Implant. Dent. Relat. Res. 7 (2005) s76–s82, https://doi.org/10.1111/j.1708-8208.2005.tb00078.x.
[49] B. Chehroudi, D. McDonnell, D.M. Brunette, The effects of micromachined surfaces on formation of bonelike tissue on subcutaneous implants as assessed by radiography and computer image processing, J. Biomed. Mater. Res. 34 (1997) 279–290, https://doi.org/10.1002/(SICI)1097-4636(19970305)34:3<279::AID-JBM2>3.0.CO;2-H.
[50] M. Hirao, K. Sugamoto, N. Tamai, K. Oka, H. Yoshikawa, Y. Mori, T. Sasaki, Macro-structural effect of metal surfaces treated using computer-assisted yttrium-aluminum-garnet laser scanning on bone-implant fixation, J. Biomed. Mater. Res. Part A. 73A (2005) 213–222, https://doi.org/10.1002/jbm.a.30277.